A Generic Cyclist Model for aerodynamic investigation: Design, geometry & first aerodynamic analysis of a male time-trial and sprint model

Wouter Terra [a,*], Christopher Brown [b], Siward Vloemans [c], Max van der Waals [a], Andrea Sciacchitano [a], David Burton [b], Mark C. Thompson [b], Toon Huysmans [c]

[a] Department of Aerodynamics, Faculty of Aerospace Engineering, Delft University of Technology, Delft, the Netherlands
[b] Fluids Laboratory for Aeronautical and Industrial Research, Department of Mechanical and Aerospace Engineering, Monash University, Australia
[c] Department of Human-Centered Design, Faculty of Industrial Design Engineering, Delft University of Technology, the Netherlands

ABSTRACT

Research in cycling aerodynamics is performed using mannequins of different geometries, which are usually not shared, thus hampering the advancement of our understanding of the flow around a rider on the bike. The primary outcome of this work is to introduce and openly share two anthropometrically realistic generic cyclist models, one in time-trial and one in sprint position. These two models are obtained by averaging the scans of 14 male elite cyclists. The average cyclist geometries are published and openly accessible, making them unique in the field of cycling aerodynamic research. The second objective of this work is to better understand how the difference between the sprint and time-trial position affects the velocity and vortex topology in the wake of a cyclist and, in turn, the aerodynamic drag. Robotic volumetric particle image velocimetry measures the time-average velocity for each mannequin within a wind tunnel. One meter downstream of the lower back, the wakes of the two mannequins are dominated by strong hip/thigh streamwise counter-rotating vortices, which induce a downwash behind the riders' backs. The strength of these vortices downstream of the sprint model is significantly larger than that of the vortices of the mannequin in the time-trial position. The same holds for a secondary vortex pair that originates from the upper arms and hips. In addition to the vortex strength, the aerodynamic drag area of the sprint model exceeds that of the time-trial model. Hence, it is presumed that stronger vortices relate to higher aerodynamic drag. In contrast to the drag area, the drag coefficient of the two models is the same. Further research is necessary to understand the relation between the cyclist position, the flow topology and the drag coefficient. Finally, the flow around the time-trial model is described in further detail to understand the origin of the different vortex structures. Through comparison to the literature, a vortex topology classification is postulated for the mid-wake and upper-wake. The arm spacing and shoulder width play a critical role in the development of this vortex system.

1. Introduction

In the last decade, many works have appeared that deal with cyclist aerodynamics. Research mainly focused on aerodynamic drag reduction through, among others, modification of rider garment (Brownlie et al., 2009; Oggiano et al., 2013) and bike components (Jux et al., 2023), changing the rider position on the bike (Giljarhus et al., 2020) and riding in a specific formation (Blocken et al. 2013, 2018). Other studies have aimed to describe the flow topology in relation to the aerodynamic drag (Crouch et al., 2014; Brown et al. 2020, 2023; Terra et al., 2020) in order to understand what is generating the latter, which may lead to new drag reduction strategies in the future. Many of these studies use a cyclist mannequin to ensure high repeatability of the measurements. The more recent mannequins are generally obtained by scanning individual athletes, resulting in highly realistic models (e.g. Chi et al., 2020; Terra et al., 2020). Because of personal anthropometric data, the model's geometry is often not shared, thus precluding follow-up studies on the

same geometry from different research groups. Because the rider's posture dominates the large-scale flow structures and contributes to about 80% of the overall aerodynamic drag (e.g. Griffith et al., 2014), the availability of the model's geometry is essential to be able to validate results reported in the literature and build upon it to advance our understanding of the flow around the cyclist and the bike. We believe an openly shared, realistic cyclist model to be used among the cyclist aerodynamic research community would be valuable and is currently missing.

An example of the use of generic models comes from the automotive industry. The flow around the Ahmed and SAE body, rudimentary models of a car, have been studied in detail, providing insights, among others, into the formation of the wake-dominating vortex structures (e.g. Ahmed et al., 1984) and flow control methods for aerodynamic drag reduction (e.g. Aider et al., 2009; Hanfeng et al., 2016). As a consequence of the level of abstraction of these models, the former insights can only partly be used in practice, while the use of specific car models,

* Corresponding author.
  E-mail address: w.terra@tudelft.nl (W. Terra).

on the other hand, is often limited by restricted access. This led to the introduction of the more realistic DriveAer model (Heft et al., 2012). This model has a realistic contour and, among others, features different rear-end geometries (sedan, estate and fastback) and underfloor configurations (flat and detailed). More recently, variations of this model have been published, for example, the AeroSUV (Zhang et al., 2019). These different models are now commonly used in the car industry, with the geometries and results made openly accessible.

The example of the DrivAer model inspired the authors to introduce a generic model to be used by the research and industrial cycling community. General models of the human body have been used in the past by modelling the different parts of the body as being more generic bluff bodies, such as cylinders and spheres (e.g. Shanebrook and Jaszczak, 1974; Brownlie, 1992). Such models, however, are extreme simplifications of the complex geometries of human body parts. The first goal of the present work is to introduce a Generic Cyclist Model (GCM) exhibiting a realistic human geometry.

Therefore, the actual human geometry will serve as the basis to establish such a GCM and, to avoid obtaining a model with individual human features, a large population of humans will form the basis for the final model. Open-source human anthropometric software (e.g. Make Human) can obtain a reasonable model of the average human (e.g. Puelles et al., 2021). Alternatively, databases containing the anthropometric features of a large human population may be used, e.g. DINED mannequin (Huysmans et al., 2020). None of the former datasets, however, contains data of cyclists specifically. A second limitation of using such standard databases is that the human geometry would need to be articulated into a cycling position, which may lead to non-realistic deformation of the human model (Garimella et al., 2020). To avoid the latter, athletes can be scanned in their race position so that significant articulation is unnecessary.

In this work, a generic model is created by combining the geometry of a group of male elite cyclists. The riders are scanned in two positions on their bike: a time trial position on their time trial bike and a sprint position, also referred to as the drops position, on their road bike. The rider statistics, the scanning process, the post-processing of the geometrical data and the method for averaging the geometries is described in detail. The second goal of this work is to describe the flow around the two generic cyclist models. Volumetric robotic particle image velocimetry is used to describe the velocity around a TT and sprint wind tunnel GCM. The flow around TT cyclist models has been researched in quite some detail in the literature (e.g. Crouch et al., 2014; Terra et al., 2020; Wang et al., 2022; Brown et al., 2023). Despite the similarities, discrepancies between the described wake flows (e.g. presence and strength of upper arm/hip vortices), seem to stem mainly from variations in the TT posture. This again emphasizes the need for a common cyclist model with known geometrical properties. Apart from the TT model, Wang et al. (2022) also investigated the flow around a cyclist sprint model through numerical simulations. Wind tunnel experimental data, however, is missing in the literature. Hence, the present TT and sprint model flow topologies are compared among each other and to the literature to better understand the impact of rider posture on the flowfield around it.

Essential to this work is that the generic cyclist models are anthropometrically realistic and representative of a wide range of professional cyclists, rather than reproducing the specific anthropomorphic characteristics of individual riders. Furthermore, it is considered crucial that the generic cyclist model geometries, together with the measured flow fields, are published and can be accessed openly, so that research groups can freely use them for further wind tunnel experiments and numerical simulations, thus allowing advancing the scientific research on cycling aerodynamics. These unique features make the GCMs superior over other models reported in the cycling aerodynamic literature. The authors realize that the two cyclist positions investigated here are quite limited in relation to the many variations reported in the literature (e.g. Malizia and Blocken, 2021) and observed in practice. Also, the leg

position of the two models is fixed, while it is well-known that the leg position largely governs the topology of the rider's wake and significantly affects the aerodynamic drag (Crouch et al., 2014). The present models should be considered as a start of developing a wider range of model variations, similar to the development of the DrivAer, which will include, among others, different leg positions and a female GCM. This future vision of the authors is addressed in more detail in the discussion section in the end of this work. Finally, note that the present GCMs represent elite cyclists that nowadays participate in competition. When the general rider's body shape or position on the bike changes significantly in time, introducing up-to-date GCMs might be necessary in the future.

2. The design of the generic cyclist models

The process followed to construct the GCM is based on the DINED mannequin (Huysmans et al., 2020) and consists of six steps, visualised in Fig. 1: Select riders, Capture riders by scanning, Process the scan data, Correspond the individual models to one another to, afterwards, Average the individual rider geometries, and finally post-process the geometry for manufacturing.

Select riders: Cyclists can be categorized into different types. In this work, one rider type is considered, namely the endurance rider. Further differentiation between riders in sub-categories or specialisations is also possible, such as sprinters, punchers, climbers and general classification (GC) riders etc. In this work, we did not make such a distinction. In addition to the rider type, a rider can take different positions or postures on a bike. Well-known postures are the upright, drops, handlebars and time-trial position. Both the rider type as well as the rider posture significantly affect the rider's drag coefficients and, presumably, the topology of the flow. We aim to introduce generic cyclist models of a certain type and posture and, therefore, only riders of that specific combination are considered to build the average models. Hence, the generic models introduced in this work are representative of a specific category only. Furthermore, only professional athletes are considered in the rider selection process, assuming that cyclists exhibit specific anthropometric characteristics that differ from the average person. Commonly, endurance cyclists compete on the road as well as the track and, so, any of these riders are considered for participation in this work. Finally, only male riders have been considered, assuming that body composition and in turn the flow around it depends on gender. A female GCM is planned for future work. The fourteen riders who participated in this work have been anonymously listed in Table 1. All participants provided informed consent prior to scanning and were aware that they could withdraw from the study at any moment.

Capture riders: Each rider is scanned statically in his race position, the left leg stretched and the right leg retracted, seated on his bike, which was installed on a bike trainer, wearing their regular cycling kit (e.g. bib, jersey, shoes) except for a helmet. Before scanning started, riders warmed up 2–3 min on the trainer to get into their natural position. Then, scanning started, which took about 4 min for each rider in one position. Two persons scanned the rider, one from the left and one from the right, maintaining some overlap and using structured-light Artec Eva handheld 3D scanners, commonly used for scanning human subjects (e.g. Garimella et al., 2020; Chi et al., 2020). Scanning with two people decreased scanning time and the consequent problems of in-scan displacements due to rider movement. All participants are scanned in time-trial posture on their TT bike and ten of them were also scanned in sprint position on their road bike.

Process scans: The captured data consist of point clouds that are post-processed in ARTEC Studio 12 (ARTEC 3D, 2017). This procedure involved, among others, removing parts that are not the cyclist (e.g. bike, floor; Fig. 2a) and aligning multiple scans into one (e.g. scan data from the left and right side of the rider) and conversion into a watertight surface through a smooth fusion (Kazhdan and Hoppe, 2013). The alignment and fusion was complicated by in-scan rider movements
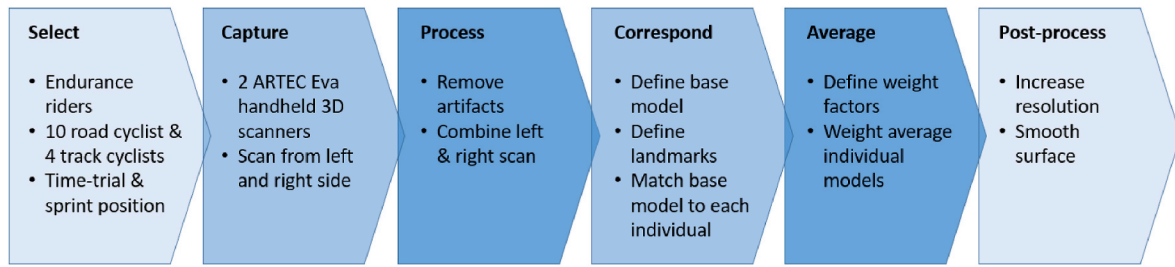
Fig. 1. Flow chart of the process defining the two Generic Cyclist Models.

Table 1
Characteristics of the riders used for the Generic Cyclist Models.

Rider #	Main type of competition	Specialisation	Scan position	Weight [kg]	Height [cm]	Weight factor [%]
01	Road	Climber	TT & SPRINT	63	172	5.1
02	Road	Climber/GC	TT & SPRINT	65	179	7.1
03	Road	Climber/puncher	TT & SPRINT	67	179	8.8
04	Road	Puncher	TT & SPRINT	68	179	9.5
05	Road	Classics/sprint	TT & SPRINT	70	179	10.4
06	Road	GC	TT & SPRINT	71	189	10.5
07	Track	TimeTrial/climber	TT	72	182	10.3
08	Road	Time-trial/classics	TT & SPRINT	75	188	8.5
09	Road	Time-trial	TT & SPRINT	75	190	8.1
10	Road	Time-trial/climber	TT & SPRINT	76	179	7.6
11	Track	TimeTrial/sprint	TT	78	176	5.7
12	Road	Classics	TT & SPRINT	79	184	4.8
13	Track	Time Trial/classics	TT	82	182	2.4
14	Track	TimeTrial/sprint	TT	85	192	1.0

(a) Raw data

(b) Fusion

alignment artifact

(c) Landmarks on template mesh

(d) Mesh corresponded to scan
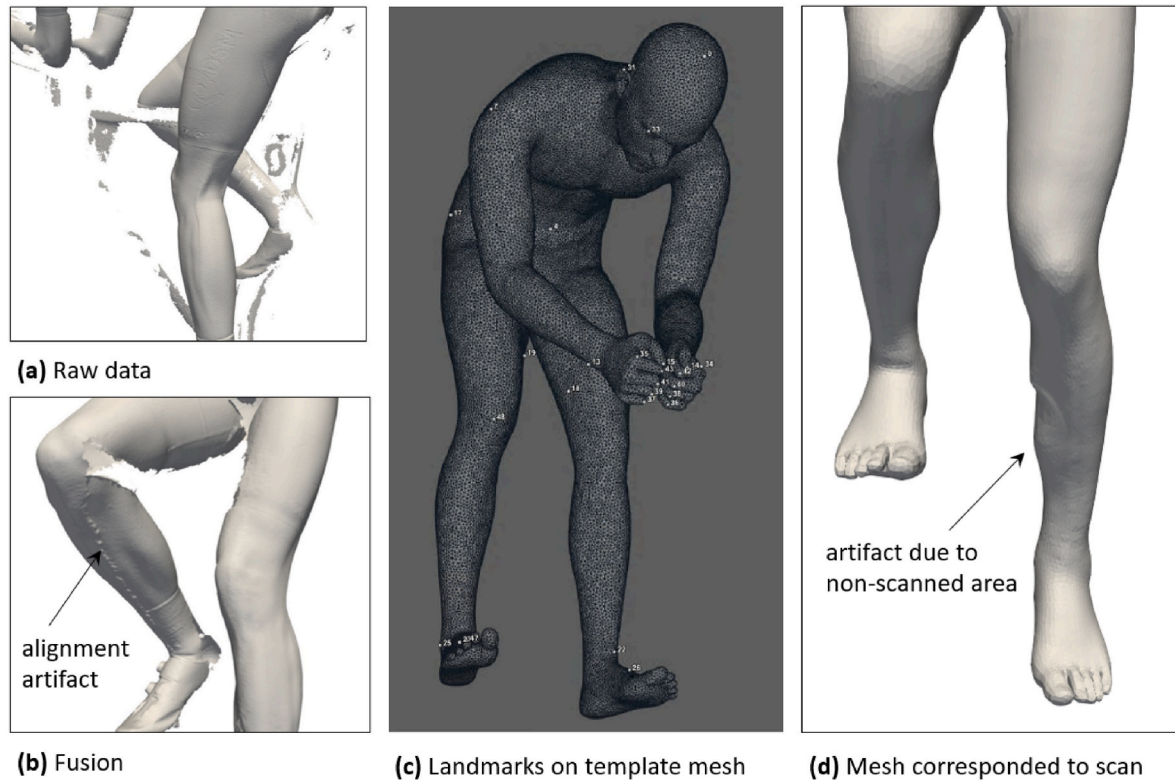
artifact due to non-scanned area

Fig. 2. Scan data: from point clouds to a mesh.

(Fig. 2b), which were more prominent in the sprint position because of the lack of elbow rests. The mesh was exported in.OBJ format.

Correspond base mesh to individual models: In order to average the scans, a base (surface) mesh was associated to each individual scan in R3DS wrap. The base mesh, highlighted in Fig. 2c, had 40 manually defined landmarks at meaningful geometric locations. This base mesh is rigidly registered to the individual scans by first aligning the manually defined landmarks using the Rigid Alignment Node Algorithm and

second non-rigidly deforming the aligned base mesh to match the geometry of the rider (Dyke et al., 2020). Due to the limited definition of hands and feet, they were only allowed to align and scale globally with the non-rigidly deforming body, resulting in hands and feet largely resembling those of the template. The registration method can result in possible joint deformations. Wrapped models' deformations are smoothed using the DeltaMush Algorithm (Mancewicz et al., 2014), resulting in smooth deformations while retaining surface details.

The resulting individual wrapped models cannot be displayed in detail as they could be traced back to the actual professional riders. Nevertheless, the variation in sprint position among the participants can be appreciated from the side view of the wrapped models in the corresponding posture (Fig. 3a). In addition, the horizontal intersections, at the height of the right knee, of the participants in TT posture (Fig. 3b) provide an indication of the variation in the upper leg geometry. Despite the differences among the riders, no evident outliers are present in the postures and the leg cross-sectional geometries.

Average individual models: The scans of the individual riders are averaged in order to produce the Generic Cyclist Model. A weighted average is computed. The weight factor, WF of scan i depends on the weight, w_i [kg] of the corresponding rider relative to the average rider weight, $\overline{w}$ of the larger population of cyclists that is assumed to be normally distributed:

$$WF_i = \frac{1}{\delta\sqrt{2\pi}} e^{-\frac{\left(\frac{w_i - \overline{w}}{\delta}\right)^2}{2}}$$

The group of cyclists that participated in the London Olympic road race is the representative population (Wood, 2015) with an average weight $\overline{w} = 70.8$ kg and a standard deviation $\delta = 6.55$ kg. After computation of the above weight factors, they are normalized to sum up to unity. Weighted averaging, in contrast to averaging with equal weights, is used to obtain a model that is more representative to the general population and avoids a significant bias of the mean as a consequence of the relatively small sample size.

Post-process average: In the last step, the average models are post-processed to enhance their surface quality. The mesh was subdivided (Paraview) to decrease the size of the surfaces' faces and, afterwards, a global smoothing (MeshMixer) was applied to the entire model excluding the hands, feet and the face. Across the majority of the mannequin, the global smoothing resulted in a surface displacement below 0.1 mm. The maximum surface displacement of 5 mm occurred in regions with high surface curvature (e.g. small parts of the inner knee and inner elbow). Fig. 4 depicts the two GCMs in time-trial and sprint positions and Table 2 lists their main characteristic dimensions. Apart

from the obvious difference in the arm posture, it is observed that the TT model, in comparison to the sprint model, exhibits almost the same trunk angle (14° vs 16°). However, the entire body is rotated further forward, resulting in a smaller angle of the upper leg (12° vs 18°). Furthermore, the head of the TT model is held lower relative to the shoulder height. The average and standard deviation of the underlying individual rider ensemble of the torso length and elbow width have also been included, providing again some insight into the variation among the rider participants. The good match between the GCM dimensions and the average of the underlying ensemble also demonstrates the validity of the averaging procedure of the individual scans. The original GCM.STL files are available at the 4TU repository (Terra et al., 2024).

3. Experimental setup and procedures

3.1. Experimental apparatus

The experiments are conducted in the atmospheric closed-circuit Open Jet Facility (OJF) wind tunnel of the Aerospace Engineering Laboratories of the Delft University of Technology. The OJF features an area contraction ratio of 3:1 and an octagonal nozzle of 2.85×2.85 m². The OJF operates at freestream velocity ranging from 4 to 35 m/s. The free-stream turbulence intensity is below 1% (Lignarolo et al., 2014).

Two full-scale wind tunnel cyclist mannequins are produced through additive manufacturing, replicating the TT and Sprint GCM geometry introduced in the previous section. A PUTOP primer is applied to each model and then manually polished with sandpaper (grain 400), thus establishing a smooth model surface. The wind tunnel models' arms and legs can be disassembled to allow testing with garments in the future. In the present work, the cyclist models did not wear suits. Dressing the mannequins in specific cycling apparel would complicate the reproduction of the results by others, both experimentally and numerically. During the wind tunnel tests, the seams between the limbs and the torso were covered by insulation tape. The TT model is installed on a Scott Plasma 5 frame with rim brakes, a Shimano DuraAce wheelset and it is wearing a Kask Mistral helmet. The sprint model sits on a Scott Addict RC frame featuring disc brakes and a Vision SC 40 wheelset. It is equipped with a Kask Bambino helmet. Both models wear Shimano S-Phyre RC902 shoes (size 44). Fig. 5 depicts side-views of the scans of the two wind tunnel models, while Fig. 7 shows the models installed on the wind tunnel platform. The bikes are fixated at the front and rear axle and are installed onto a false floor, elevated 20 cm above the wind tunnel contraction exit, to reduce the boundary layer interacting with the model.

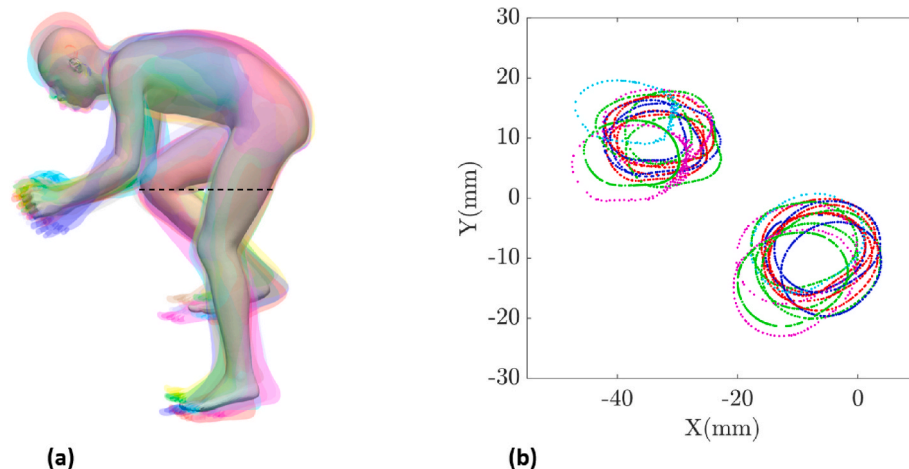To quantify the difference between the physical cyclist models and

(a)

(b)

Fig. 3. **a** Side view of the scans of the individual participants in sprint position (coloured transparent meshes) overlaid on top of their average geometry (grey solid mesh) and **b** intersections of the individual participants in TT posture (indication of location marked by dashed black line in figure a).
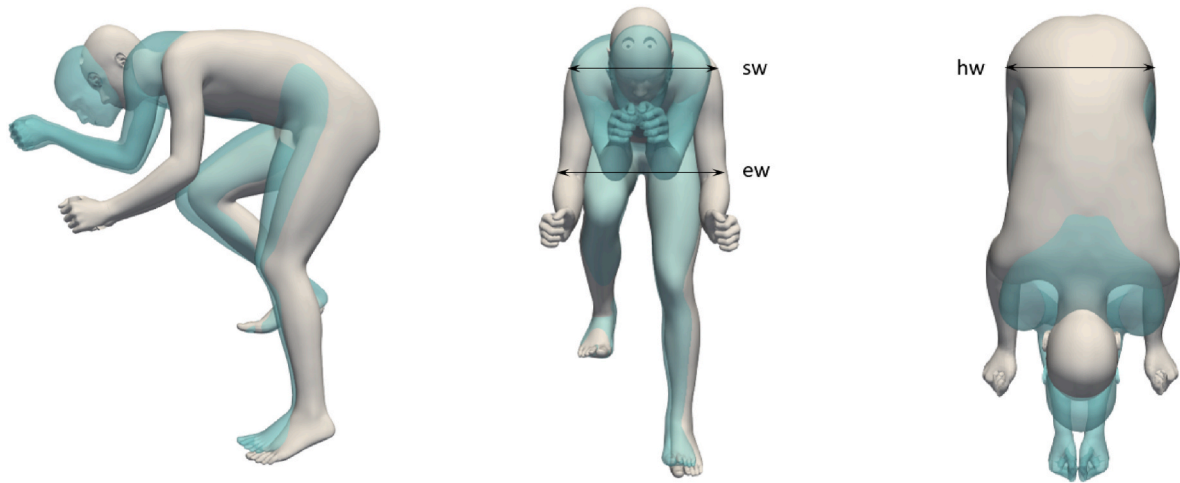
Fig. 4. Parametric views of the TT GCM in green and the sprint GCM in grey. For better readability, the definition of the characteristic body angles is depicted in Fig. 5.
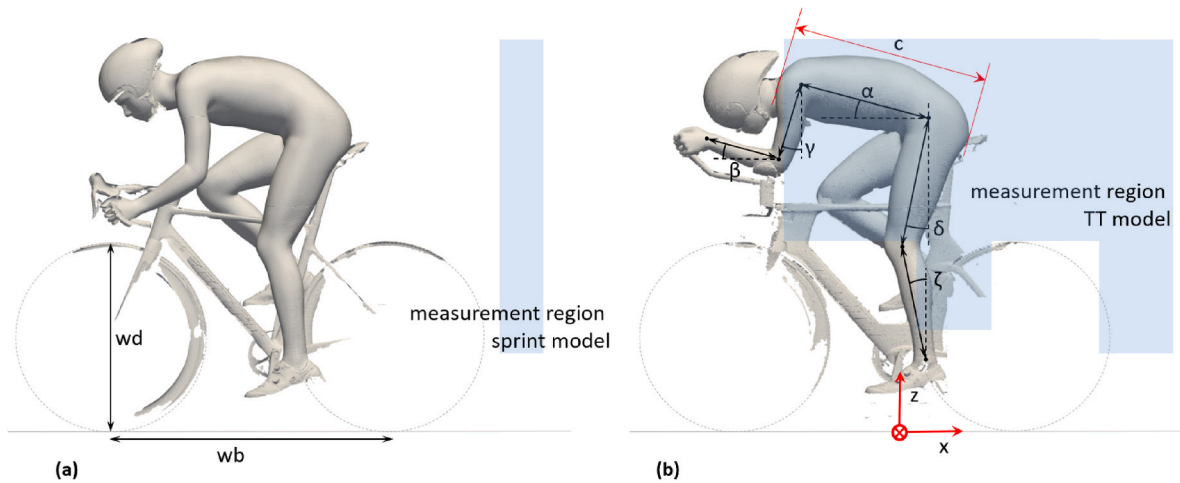

Fig. 5. Partial scans of the mannequins and their bikes: **a** the sprint position and **b** the TT position.

the digital counterparts, the former are scanned (ARTEC EVA hand scanner), and the scans are overlaid with the latter. Fig. 6 depicts the closest point distance between the two. Because the wind tunnel model was scanned sitting on the bike wearing a helmet and shoes, large offsets are present at the head and the feet. Other peaks in the offset between the models result from areas of the physical mannequin that were not scanned, e.g. the inside of the stretched leg, the right knee and the backside of the right upper arm. The disparity between the two models remains well below 4 mm along the remainder of the body. Only at the front and back of the lower left leg, the offset exceeds 4 mm with values around 10 mm. This is attributed to a slight misalignment in the connection between the lower leg and the upper leg in the connection just above the knee (visible in the scans of the models in Fig. 5). The excellent similarity between the physical and digital TT model is representative for the Sprint GCM as well. The scans of the mannequins on their corresponding bikes are available at the 4TU repository (Terra et al., 2024).

3.2. Particle image velocimetry system, procedures and data reduction

Robotic volumetric particle image velocimetry (Jux et al., 2018) is employed to measure the air velocity around the GCMs. Sub-millimeter, neutrally buoyant Helium-filled soap bubbles are used as flow tracers. An in-house developed seeding system operates a total of 400 HFSB

generators that are integrated into 20 vertically oriented wings, installed in a staggered formation onto an arc-shaped base that integrates the supply lines of air, soap and helium. The seeder is located in the OJF's settling chamber (Fig. 7) and spans an area of 1m (width) × 2m (height); considering that the wind tunnel contraction area ratio is 3, the resulting seeded streamtube in the test section is approximately 0.6m × 1.2m. The arc-base of the seeding generator is 40 cm high and the false ground of the wind tunnel platform is elevated about 15 cm above the floor of the OJF nozzle to remove the established boundary layer; hence, the first 10 cm from the platform floor remains without seeding. The HFSB generators in the upstream and downstream vertical wings can be operated separately; during the present experiments, only the 200 generators of the downstream wings were used, resulting in an estimated total bubble production of 6 million bubbles/s and a concentration of 0.6 bubbles/cm^3. The presence of the seeding system increases the freestream turbulence intensity from 0.5% to approximately 0.8% (Giaquinta, 2018).

The LaVision GmbH *Minishaker Aero CVV* probe houses four CMOS cameras and an optical fibre. The latter transmits and distributes the laser light produced by a Quantronix *Darwin Duo* Nd:YLF laser (25 mJ pulse energy at 1 kHz) resulting in a conical-shaped measurement region. A 6-degree-of-freedom Universal Robots A.S. *UR5* robotic arm translates and rotates the CVV probe with a positional repeatability of ±0.03 mm and ±0.01°, respectively, allowing to scan the time average

Table 2

Main characteristics of the GCMs. The definition of the angles is depicted in Fig. 5.

name	Symbol	Position/length			
		TT position		Sprint position	
		GCM	ensemble of underlying individual models Average ± standard deviation	GCM	ensemble of underlying individual models Average ± standard deviation
Torso angle of attack	α	14°		16°	
Lower arm angle	β	13°		−30°	
Upper arm angle	γ	16°		0°	
Upper leg angle	δ	12°		18°	
Lower leg angle	ζ	11°		11°	
Torso length	c	700 mm	690 ± 24 mm	650 mm	655 ± 23 mm
Shoulder width	sw	370 mm		400 mm	
Elbow width	ew	210 mm	210 ± 24 mm	460 mm	455 ± 18 mm
Hip width	hw	335 mm		335 mm	
Wheel base	wb	995 mm		1010 mm	
Wheel diameter	wd	680 mm		680 mm	

flow on one side of the cyclist, from its head to just downstream of the rear wheel. To reach the flow on the other side of the cyclist, the PIV system is moved from the left side of the mannequin (depicted in Fig. 7) to the right side. Aerodynamic interference effects from the robotic PIV system are generally within 2% (Giaquinta, 2018). The main specifications of the PIV system are summarized in Table 3.

All PIV measurements are conducted at a freestream velocity $U_\infty = 14$ m/s, representative of the speed in elite road cycling races. In each position of the optical head, 10,000 image quadruples are acquired at a frequency is 821 Hz. For the TT model, images are acquired at approximately 100 different positions of the optical head almost all around the model (area marked light blue in Fig. 5b), while for the sprint model the measurements were limited to 16 different positions within a

rather thin volume just downstream of the rear wheel (Fig. 5a). The flow velocity information is retrieved via Lagrangian Particle Tracking (Shake-the-Box algorithm, Schanz et al., 2016, in the LaVision DaVis 10 software) after mitigating the background noise and reflections in the acquired PIV images. Velocity statistics are obtained from the Lagrangian velocity ensemble, combining all CVV probe positions, within cubic bins of $4.5 \times 4.5 \times 4.5$ cm^3 with 75% overlap requiring at least 20 particles per bin. Hence, the vector spacing in x, y and z direction of the GCM velocity datasets, published online, is about 11 mm.

The resulting time-average velocity, $\overline{U} = \{u, v, w\}$ is presented in non-dimensional form ($\overline{U}^* = \overline{U}/U_\infty$) in the right-handed coordinate system $\{x, y, z\}$ with its origin located at the bike's centerline at ground level (Fig. 5b). The non-dimensional streamwise vorticity is calculated as $\omega_x^* = (\nabla \times \overline{U})_x L/U_\infty$, with L the hip width of the mannequin. The velocity uncertainty, ε_u partly stems from the flow unsteadiness and the PIV random errors. The relative random uncertainty at 95% confidence level is evaluated as $\varepsilon_u = k\sigma_U/(U_\infty\sqrt{N_t})$, σ_U being the velocity standard deviation, k = 1.96 the coverage factor and N_t the number of tracks per bin. In the freestream ($N_t > 1000$; $\sigma_U/U_\infty \sim 0.11$) and the near-wake of the upper leg ($N_p > 100$; $\sigma_U/U_\infty \sim 0.4$) the uncertainty values are approximately 0.7% and 8%, respectively. Along the boundary of the measurement domain, at the edge of seeded and non-seeded flow, the velocity error is significantly higher, which is magnified in the computed vorticity, as it will be discussed in the results section. To exclude regions with uncertainties above 10%, the presented velocity data (and published) is cropped to -240 mm $< y < 240$ mm.

In addition to the uncertainty, the presence of the CVV probe, the robotic arm and its supporting structure affect the flow around the cyclist models. For a similar robotic volumetric PIV apparatus, the freestream flow interference is reported to be approximately 1% for an imaging distance of 32 cm and an angle of 90° between the freestream direction and the imaging axis (Giaquinta, 2018). Proximity effects on the velocity and vorticity downstream of a simplified car model, at 40 cm between the CVV probe and the wind tunnel model, are reported to be below 1% and 5%, respectively, and are considered representative for the present measurements. The proximity effects will be further quantified in a follow up work, that compares the present wake velocity information to that acquired through scanning the wake with a 4-hole probe.

Finally note that during the measurements, the mannequins were slightly vibrating as a consequence of the interaction with the air. The bottom of the bike was fixated and did not move. Instead, the top of each mannequin was moving by about 1 cm from the left to right (along y). This mannequin motion generally widens the wake and reduces the peak
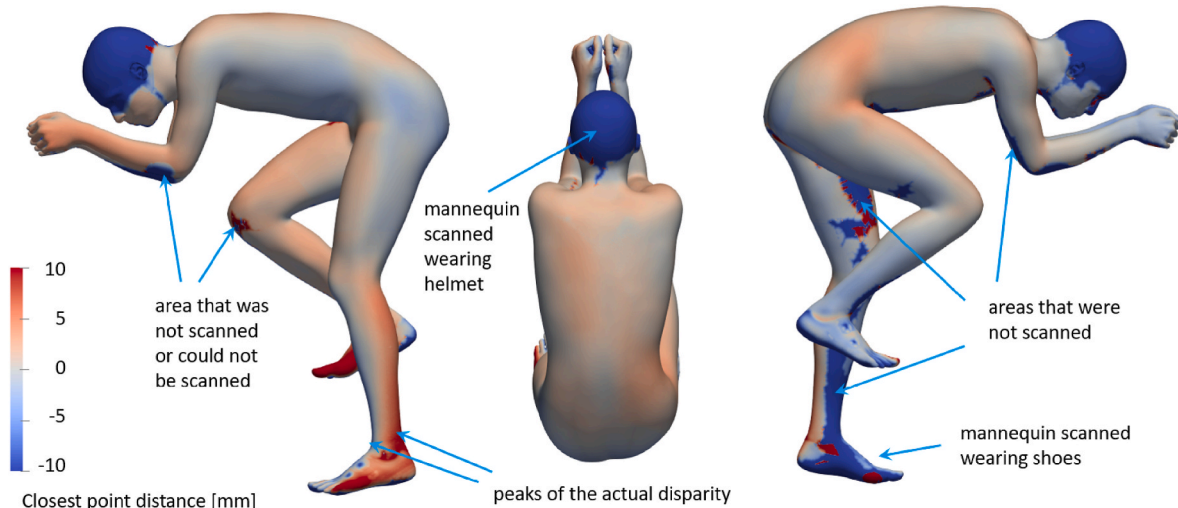

Fig. 6. Comparison between the digital TT GCM and the scan of the corresponding physical wind tunnel model.
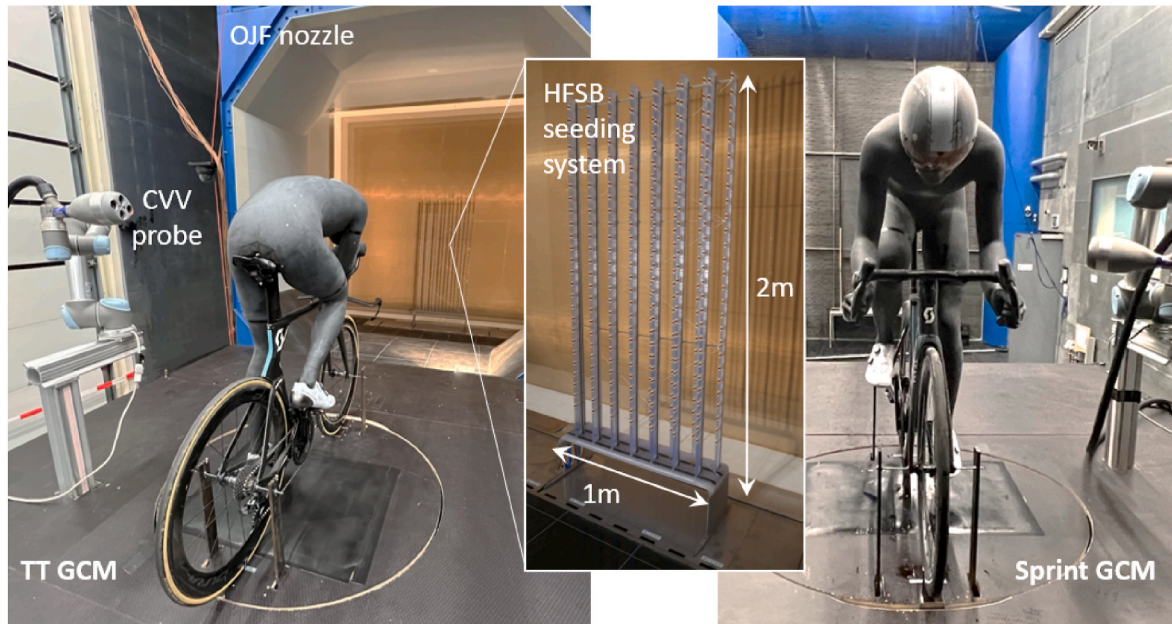
Fig. 7. Wind tunnel experimental setup: The TT (left) and the sprint model (right) including the robotic volumetric PIV measurement components.

Table 3
Coaxial Volumetric Velocimeter specifications.

Optics	Focal length	4 mm
	Cameras numerical aperture	11
Imaging	Tomographic aperture (horizontal, vertical)	4°, 8°
	Sensor size	640×476 px^2
	Pixel pitch	4.8 μm
	Maximum acquisition frequency	821 Hz
	Bit depth	10
Illumination	Nominal pulse energy	25 mJ
	Wavelength	527 nm

velocity and vorticity. However, because of its relatively small amplitude in relation to the size of the mannequin, the effect on the velocity field is small, in particular at some distance downstream of the model.

3.3. Force balance measurements

Force measurements are carried out with a six-component balance designed, manufactured and calibrated by the Dutch Aerospace Laboratory (NLR). The balance is connected through four vertical struts to the bike's front and rear wheel axles; a false floor shields it from the wind tunnel jet. The aerodynamic drag D and lift L are measured in a range of freestream velocity between 4 m/s and 26 m/s. The aerodynamic drag area $C_D A$ and lift area $C_L A$ are calculated as:

$$C_D A = \frac{D}{1/2 \rho U_\infty^2},$$

$$C_L A = \frac{L}{1/2 \rho U_\infty^2},$$

where ρ [kg m^{-3}] is the air density and A [m^2] is the frontal area of the wind tunnel model. The frontal areas of the TT ($A_{TT} = 0.35 \pm 0.01$ m^2) and the sprint model ($A_{sprint} = 0.41 \pm 0.01$ m^2), including the corresponding bikes, are obtained from the digital scans. These scans do not contain the entire bike, thogh, and, so, the missing part of the frontal area was estimated based on photos, which is the reason for the relatively high frontal area uncertainty. The uncertainty of the measured aerodynamic drag stems from the accuracy of the balance, the unsteady nature of the cyclist's aerodynamic drag and the variation in model

geometry throughout repeated installations of the mannequin and bike in the wind tunnel. The balance maximum error of the measurement of the streamwise loads is 0.15 N, while the relative uncertainty of the time-average aerodynamic drag, measured for 30 s at a frequency of 2 kHz, is conservatively estimated at 0.8%. The repeatability error of the aerodynamic lift and drag measurement are between 6% and 2%, being the difference between the minimum and maximum value measured over three model installations relative to the corresponding absolute aerodynamic drag value. The large relative error in the lift area is because the absolute value of the lift area is a factor 10 below that of the drag area. Finally, the aerodynamic drag of the supporting structure is measured in isolation across the entire Reynolds number range, and subtracted from the corresponding overall force. A wind tunnel blockage correction is omitted, as the error in the correction for an open jet wind tunnel measurement, the present complex geometry and a model blockage of about 4% might be of the same order of magnitude as the correction itself (Barlow et al., 1999).

4. Results

4.1. Aerodynamic forces of the sprint and TT model

The drag area, $C_D A$, drag coefficient, C_D and lift area, $C_L A$ of the two generic cyclist models are presented against wind speed in Fig. 8. For better readability, the error bars are only included at $U_\infty = 7$ m/s. This uncertainty is representative across the Reynolds number range tested. Considering the drag area first, it is observed that $C_D A$ monotonically decays for both models over the entire velocity range and drops by about 15% between 4 and 26 m/s. This Reynolds number effect is partly caused by the boundary layer transition over the cyclist's arms and legs at increasing speed, resulting in delayed separation and, in turn, a reduction of the aerodynamic drag of these limbs (e.g., Terra et al., 2020). It is expected that at speeds beyond the current range, the drag area stops decreasing and, instead, starts increasing. This condition at which the drag areas reach a minimum depends, among others, on the freestream turbulence intensity and the surface roughness of the model (Brown et al., 2023). The monotonic decay of the aerodynamic drag is comparable to that of the cyclist replica used by Terra et al. (2019), which is in a position that is similar to the current TT GCM. For a bare mannequin at a comparable turbulence intensity level, Brown et al.,
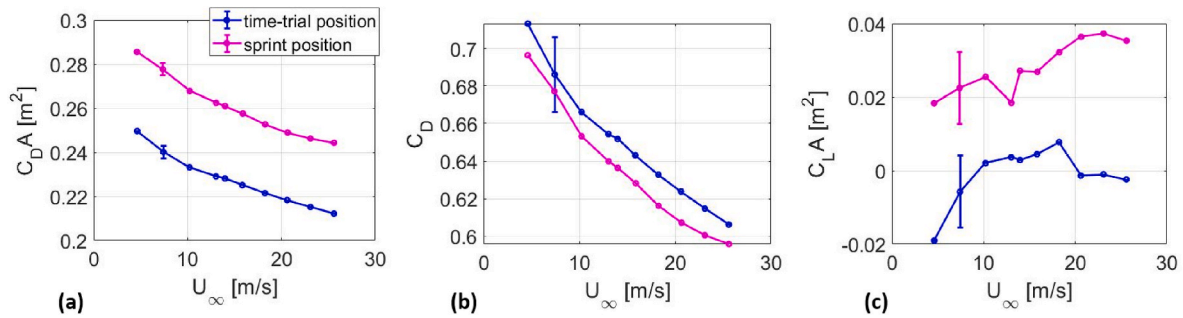
Fig. 8. Aerodynamic loads at increasing freestream velocity: **a** the drag area, **b** the drag coefficient and **c** the lift area.

(2023), instead, report a drag area that decreases and reaches a minimum around $U_\infty = 22$ m/s. Without having the exact geometry of the mannequin used in the latter work, we can only speculate on what is causing this difference. In general, the mannequins are quite alike: they have similar postures with the arms on the handlebar and do not wear a suit featuring a smooth model surface. A particular difference, though, is the ratio of the shoulder width over hip width R_w of their mannequin ($R_w = 1.35$) compared to the present ones (TT model: $R_w = 1.10$; sprint model: $R_w = 1.2$) and that of Terra et al., (2019) ($R_w = 1.05$). This might explain the different Reynolds number effect observed in the aerodynamic drag. The role of the geometry of the shoulders and the upper arms in the cyclist's aerodynamics is further discussed in sections 4.2 and 4.3.

The drag areas of the TT and sprint mannequin are well within the values reported in the literature (Crouch et al., 2017) and so is the difference in drag area, $\Delta C_D A = \left(C_D A_{TT} / C_D A_{sprint} - 1\right) \bullet 100\% = 15\%$, between the time-trial and sprint model. Although the two models are installed on different bikes, it can be assumed that the gross of this difference in drag area stems from the difference in upper body posture, knowing that the rider contributes to over 80% of the total aerodynamic drag of the bike and rider together, which is further discussed in the next section. Interestingly, the difference in frontal area between the two models is 15%, so, both models feature the same drag coefficient (Fig. 8b). The larger uncertainty of the drag coefficient stem from the uncertainty in the estimated frontal area. The negligible difference in drag coefficient compares relatively well to what is reported in the literature (e.g. Gibertini and Grassi, 2008: 3%, Wang et al., 2022: 1%). Another interesting observation is that the difference in drag area/drag coefficient is largely independent of the freestream velocity, which suggests that cyclist flow Reynolds number effects are relatively independent of the athlete posture.

Similar to the drag area, the lift area (Fig. 8c) of the sprint model is consistently higher than that of the time-trial one, suggesting that the amount of downwash created over the back of the sprint model exceeds that of the mode in time-trial position (Brown et al., 2023). Although the uncertainty of the measured lift coefficient is relatively high, the lift area values and their trend with increasing freestream velocity are similar to what is reported by Brown et al. At lower Reynolds numbers, $C_L A$ generally increases with increasing speed, it reaches a maximum and afterwards remains constant or decays. The similarity in the $C_L A$ evolution between the sprint and time-trial models, again, suggests that the Reynolds number effects between the two positions are well comparable.

4.2. The wake flow topology of the sprint and TT model

A main characteristic of the cyclist's wake is the downwash over the model's lower back that interacts with, among others, a counter-rotating streamwise vortex pair emanating from the hip and inner thighs (Crouch et al., 2014; Jux et al., 2018). Note that it is not always apparent to what extent these vortices emerge from the hips or the thighs, and interactions

occur between them as is demonstrated in the following sections. Here, we will refer to these vortices as hip/thigh vortices. Fig. 9 presents streamwise velocity (left) and vorticity (right) contours, overlaid with in-plane vectors, in a cross-plane 900 mm downstream of the bottom bracket ($x = 0$) of the two generic cyclist models. The characteristic downwash is clearly observed in the center of the wake of both models. This negative vertical velocity is significantly stronger and located at smaller z-value for the sprint model ($w^* = -0.27$ around $z = 850$ mm) than it is for the TT model ($w^* = -0.17$ around $z = 950$ mm). This difference in downwash magnitude corresponds to the difference in lift area reported before.

The peak velocity deficit downstream of the hips and upper legs of the two models are of the same magnitude ($u^* = 0.55$), only located at a different y-position (Fig. 9a). The peak value downstream of the sprint model is located around ($y = -50$ mm; $z = 750$ mm), while that of the TT model is located around ($y = 30$ mm; $z = 900$ mm). This is the consequence of the aforementioned difference in downwash strength. The downwash of the sprint model is not only stronger, it is also tilted to the right (positive y), which may explain why the velocity deficit downstream of the bended (right) leg of this model is higher than that of the TT model.

In Fig. 9b, in addition to the contours of vorticity, vortex regions are depicted (marked by the dashed line), which have been identified through application of the Q-criterion. A threshold of $Q = 150$ s^{-2} is used to identify the vortex boundaries. In addition to the stronger downwash, it is obvious that also the strength of the counter rotating vortex pair emanating from the hips and inner thighs of the sprint model ($\omega^*_{x,max} = \pm 2.1$) exceeds that of the TT model ($\omega^*_{x,max} = \pm 1.6$). As the torso angles of attack of both models are nearly the same (difference of 2°, see Table 2), the difference in vortex strength is presumably the consequence of the different positioning of the arms. It is hypothesized that a larger spacing between the arms allows air with higher momentum to access in between the arms, reach the chest area and, in turn, the gap between the two inner thighs. This air flow through the two thighs is feeding the hip/thigh vortices. Hence, a larger arm spacing results in stronger hip/thing vortices.

The intake of high momentum air in-between the arms may also explain the presence of the secondary vortex pair in the wake of the sprint model, marked as hip/upper arm vortices in Fig. 9b. In section 3.3, it is described in more detail how the shear layers emanating from the upper arms roll up around the torso and detach from the hips, resulting in the hip/upper arm vortices. This large swirling motion, from beneath the chest, around the flanks of the torso and over the hips, is also fed by the air accessing the gap between the arms. The upwash around the flanks is presumably related to the point of separation of the hip/upper arm vortex: A stronger upwash results in a point of separation of the vortex that is further upstream and further on top of the lower back in comparison to a weaker upwash. When the hip/upper arm vortex detaches higher on top of the back, it is less likely to merge with the hip/inner thigh vortex. In other words: a larger arm spacing increases the vertical distance between the hip/upper arm and hip/thigh
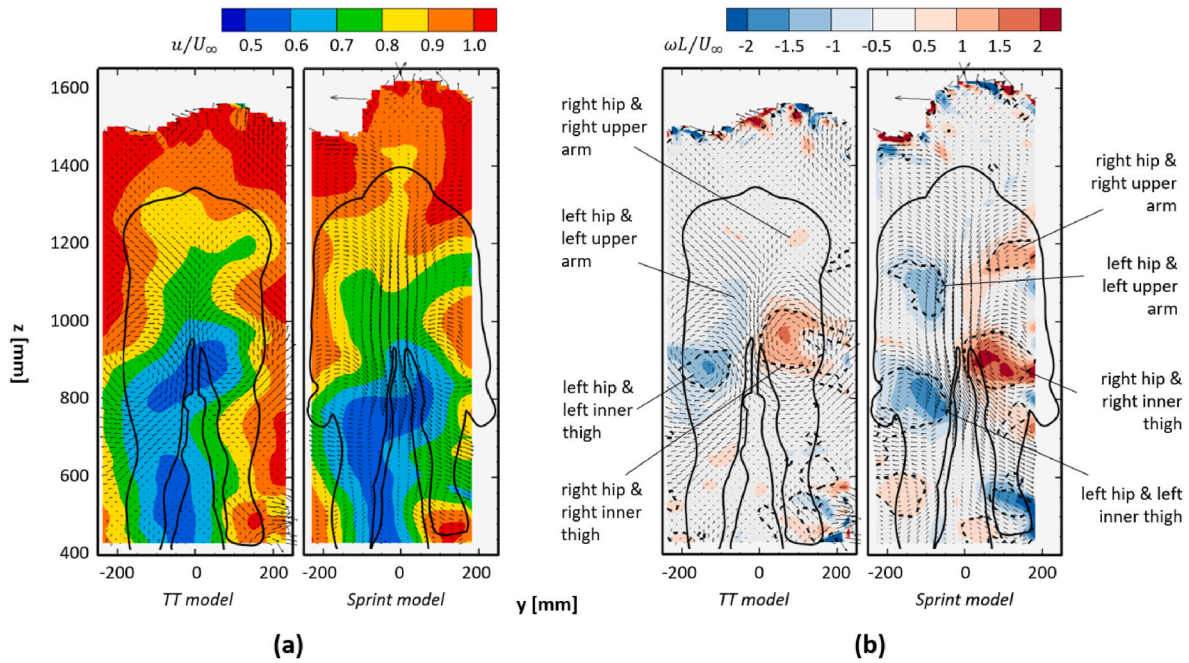
Fig. 9. a Contours of streamwise velocity and, **b** vorticity of the two GCMs at $x = 900$ mm. Dashed lines represent Q = 150 s^{-2}.

vortices and the two remain separated over a larger streamwise distance until they eventually merge. Because the arm spacing of the TT model is relatively small, the hip/upper arm vortices merge with the inner thigh vortices shortly after separating (the remainder of the latter are labelled in Fig. 9b), while these vortices of the sprint model remain separated at least until $x = 900$ mm.

Apart from the hip/upper arm vortex pair, other velocity and vorticity distributions differences are observed in the upper wake ($y > 1100$ mm) of the two cyclist models. The wake of the sprint model is wider than that of the TT model and the velocity deficit downstream of the helmet is more pronounced (Fig. 9a). The latter is most likely caused

by the difference in head position and helmet shape. The wider and taller wake of the sprint model relates well to the high aerodynamic drag of this model compared to the TT model. At the top edge of the measured region, the edge that has not been cropped, some velocity outliers are present due to lack of seeding. This velocity error is clearly amplified in the vorticity.

4.3. The GCM wake in relation to that of other cyclist models

To understand how the flow around the present generic cyclist models compares to that in existing studies, Table 4 lists the cyclist

Table 4
Dimensions of the present mannequins, and those reported in the literature, in sprint and TT position together with their dominant wake flow structures for the asymmetric leg position.

	α [°]	sw [mm]	hw [mm]	ew [mm]	γ [°]	β [°]	Vortex wake topology	Remarks
Sprint position								
GCM sprint (current)	14	400	335	460	16	13	- Hip/thigh vortex pair: downwash tilted towards bended leg - Hip/arm vortex pair: downwash	wind tunnel; no suit
Wang et al. (2022)	8	420[a]	350	480[a]	0[a]	−10[a]	- Hip/thigh vortex pair: downwash tilted towards stretched leg - Hip/arm vortex pair: upwash	CFD (DES)
TT position								
Current	14	370	335	210	16	13	- Hip/thigh vortex pair: downwash tilted towards bended leg	wind tunnel; no suit
Crouch et al. (2014)	12.5	420	350	300[a]	20	−10[a]	- Hip/thigh vortex pair: downwash tilted towards stretched leg	Wind tunnel; suit
Griffith et al. (2014)	15	420	350[b]	300[b]	20	−10[a]	- Hip/thigh vortex pair: downwash tilted towards stretched leg	CFD (LES)
Barry et al. (2016)	15	60	50[b]	300[b]	20	0[a]	- Hip/thigh vortex pair: downwash tilted towards stretched leg	Water channel; scaled model
Brown et al. (2023)	8	470	350	230[a]	19	17[a]	- Hip/thigh vortex pair: downwash tilted towards bended leg - Hip/arm vortex pair: upwash	Wind tunnel; with and without suit
Wang et al. (2022)	8	470	350	230[a]	19	17[a]	- Hip/thigh vortex pair: downwash tilted towards stretched leg	CFD
Jux et al., 2018	5	380	365	250	4	14	- Hip/thigh vortex pair: downwash tilted towards bended leg	Wind tunnel; suit

***symmetric leg position.
[a] Estimated from figures,
[b] Based on parent model**,

mannequin dimensions, and the corresponding dominating flow structures, reported in the literature. We will focus on some of the most remarkable differences. Note that this overview focuses on the cyclist in asymmetric leg position. The symmetric leg position is omitted. Wang et al. (2022) describe the flow, obtained through detached eddy simulations (DES), around a sprint model as well as a TT model, and compare the two. Although they report some unexpected results, sometimes contradicting with corresponding wind tunnel tests, we compare the present results first to those of these authors, as they are the only ones considering the cyclist sprint position. In fact, they compare the sprint and the TT position, as in the present work. Wang et al. report the counter-rotating vortex pair emanating from the hips and inner thighs as the dominating flow structure for both cyclist positions. This corresponds to the present results and the other literature (see Table 4). However, the downwash in the center of this vortex pair is not tilted towards the bent leg, as it does for the present generic cyclist models (see Fig. 9); instead, a strong tilt is present in the direction of the stretched leg. The direction of this tilt is governed by the vertical position of the two hip/thigh vortices relative to each other, together forming the counter-rotating hip/thigh vortex pair, which is illustrated in Fig. 10a by the three middle-wake variations reported in the literature: *left-tilt* (tilt towards the stretched leg), *no-tilt* and *right-tilt* (tilt towards the bended leg). Furthermore, note that the cyclist contour used in this illustration is only for a more intuitive interpretation of the vortex topology. It does not refer to a specific cyclist model. The tilted downwash towards the stretched leg is also present downstream of the cyclist models used by Crouch et al. (2014), Griffith et al. (2014) and Barry et al. (2016). These authors all used very similar models, which are based upon the same parent geometry. Nevertheless, the models are different in the sense that one is a digital model (Griffith et al., 2014), one is a model at scale 1:7 (Barry et al., 2016) and only that of Crouch et al. (2014) is a full-scale wind tunnel model. The fact that the relative orientation of the counter-rotating vortex pair is similar among these suggests that this topology is quite robust and relatively insensitive to small model variations and flow conditions (e.g., turbulence levels). The discrepancy in this vortex structure compared to the present topology, and that of Jux et al. (2018) and Brown et al. (2023), is not immediately obvious. Only the tilted downwash to the stretched leg reported by Wang et al. (2022) should be considered with some care, as the same model is used for wind tunnel tests by Brown et al. (2023) with the tilt reported in the opposite direction. It seems that wind tunnel validations remain necessary despite the use of high-fidelity numerical simulations, such as DES.

Another flow topological difference between the wake of the present sprint model and that of Wang et al. (2022) lies within the vortices emanating from the upper arms of the mannequins in both positions. In the present work, these are co-rotating with the thigh vortices, as depicted in Fig. 9b-right and illustrated in the sketch of the variations of the hip/upper arm vortex topology in the upper wake in Fig. 10b. Note, that the latter illustration considers the *no-tilt* hip/thigh vortex pair from the left figure as a basis. This does not imply that other combinations between the hip/thigh vortex topology (left) and the hip/upper arm vortex pair (right) do not exist. In contrast to the present hip/upper arm vortex topology, Wang et al. report a counter-rotating vortex pair, resulting in an upwash in the upper wake, similar to the type *upwash* in Fig. 10b. This upwash in the upper wake at about one torso length downstream of the saddle is different from the present sprint wake topology (type *downwash*), but also from the present TT topology and from that of most of the other studies using a TT model (e.g., Crouch et al., 2014; Jux et al., 2018). The latter all report an absence of significant hip/upper arm vortices at a torso length distance downstream of the saddle (upper wake type *neutral*). The presence of the counter-rotating vortex pair, however, is reported also in the wind tunnel measurement of Brown et al. (2023), who use the same model geometry as that of Wang et al. Hence, this difference in the hip/upper arm vortex pair cannot be ascribed to a phenomenon resulting from the DES but can probably be ascribed to a certain cyclist model dimension. A particular difference between that cyclist used by Brown et al./Wang et al. and the present one is the shoulder width, or the ratio of shoulder width to hip width R_w. The shoulder width was mentioned in section 4.1, when comparing the Reynolds number differences in the drag area between the two TT models. It is hypothesized that, for a cyclist with relatively broad shoulders, the outer shear layers emanating from the upper arms detach from the inner ones and roll up around the torso, forming a strong counter rotating vortex pair that, together with the thigh vortices, dominate the wake. This will be further discussed in the next section when describing the evolution of these vortices around the cyclist for the present TT model.

Altogether, many differences exist between the flow observed downstream of the present models and those reported in the literature, differences which are not all well understood. Also, the impact of the different topologies on the aerodynamic drag is unclear. For an analysis of the effect of shoulder width to hip width or elbow spacing, for example, on the wake flow topology, the present GCMs can be used. In the discussion section the authors elaborate how they envisage this. Note, finally, that the many varieties in wake topology, summarized in Table 4, apart from the differences in mannequin posture, may also stem from differences in model garment (wearing suit/type of suit) and from differences in freestream turbulence characteristics (e.g. Brown et al., 2023).

4.4. The spatial evolution of the flow around the time-trial GCM

The velocity around the body of the TT model is presented to understand, among others, where the streamwise vortices emanate from
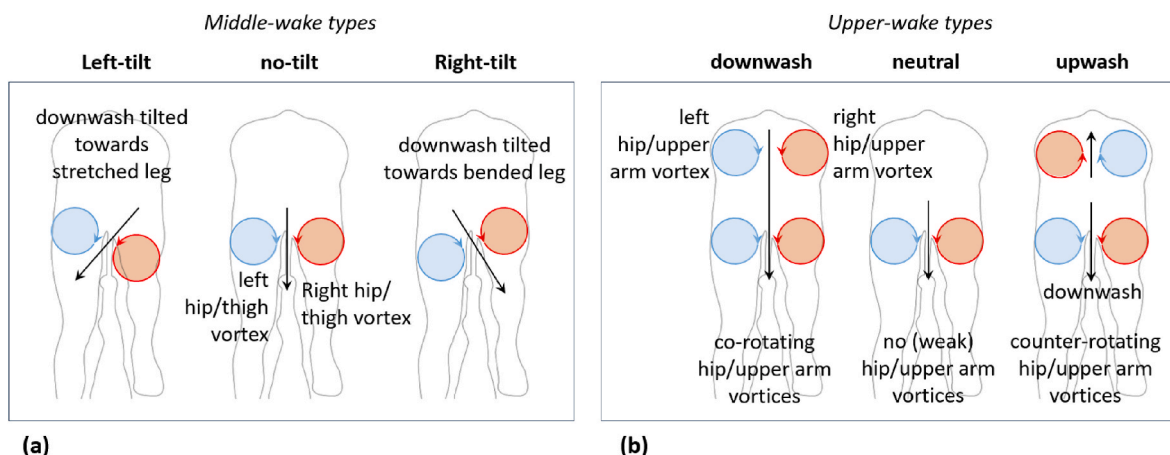

Fig. 10. Schematics of the types of hip/thigh vortex pairs in the mid-wake (left) and of the hip/upper arm vortex pair in the upper-wake (right).

the body and how they evolve and interact with other vortices downstream. Fig. 11 presents the streamwise velocity in six cross-planes starting just downstream of the upper arms ($x = -350$ mm) and ending downstream of the saddle ($x = 600$ mm). The time-trial model has not been included in the three most downstream planes for better readability of the data. In the most upstream plane ($x = -350$ mm; top-left figure) the wake of the upper and lower arms is clearly visible forming a region of reverse flow, typical for the cyclist's bluff body limbs. In addition, a distinct upwash is observed in the distribution of in-plane vectors downstream of the upper arms. We will see later that this upwash transports the separated shear layers upwards and separates them from the elbow vortices (not well visible here). The velocity distribution in the most upstream plane is rather symmetric around $y = 0$.

Further downstream, at $x = -200$ mm, the velocity deficit due to the flow separation around the arms is still visible. An asymmetry is now observed that stems from the asymmetric position of the legs: The flow approaching the knee is decelerated and the upper leg creates an additional upwash in addition to the upwash generated by the upper arms. At $x = 0$, the deceleration of the air upstream of the stretched leg is well observed, as well as the air that swirls up around the torso, forming the

start of the hip and upper arm vortices. A distinct lateral velocity component is also observed downstream the right knee, which forms because of the asymmetric leg position: the air underneath the torso is pushed to the right, away from the stretched leg; this is what becomes the right inner thigh vortex. A weak velocity deficit stemming from the helmet is also visible.

Downstream of the stretched leg, at $x = 200$ mm, a second recirculation region is observed, significantly larger than that downstream of the arms. The velocity deficit peaks downstream of the calf with a reverse velocity of $u^* = -0.35$, similar to the observations reported by the Terra et al. (2020) describing the Reynolds number effects around a TT cyclist model. The reverse flow region stretches from the lower leg to the lower back. This recirculation region closes ($u^* = 0$) about 150 mm downstream of the saddle at plane 5 ($x = 400$ mm; Fig. 11 bottom-middle). At the latter plane ($x = 600$ mm; Fig. 11 bottom-right), we observe the typical shape of the velocity deficit, with branches stemming from the left and right hip and upper arm. Also the characteristic downwash in-between these branches and the right inner thigh vortex can be clearly detected from the in-plane vectors. Fig. 12 presents the contours of the lateral (top) and vertical velocity components
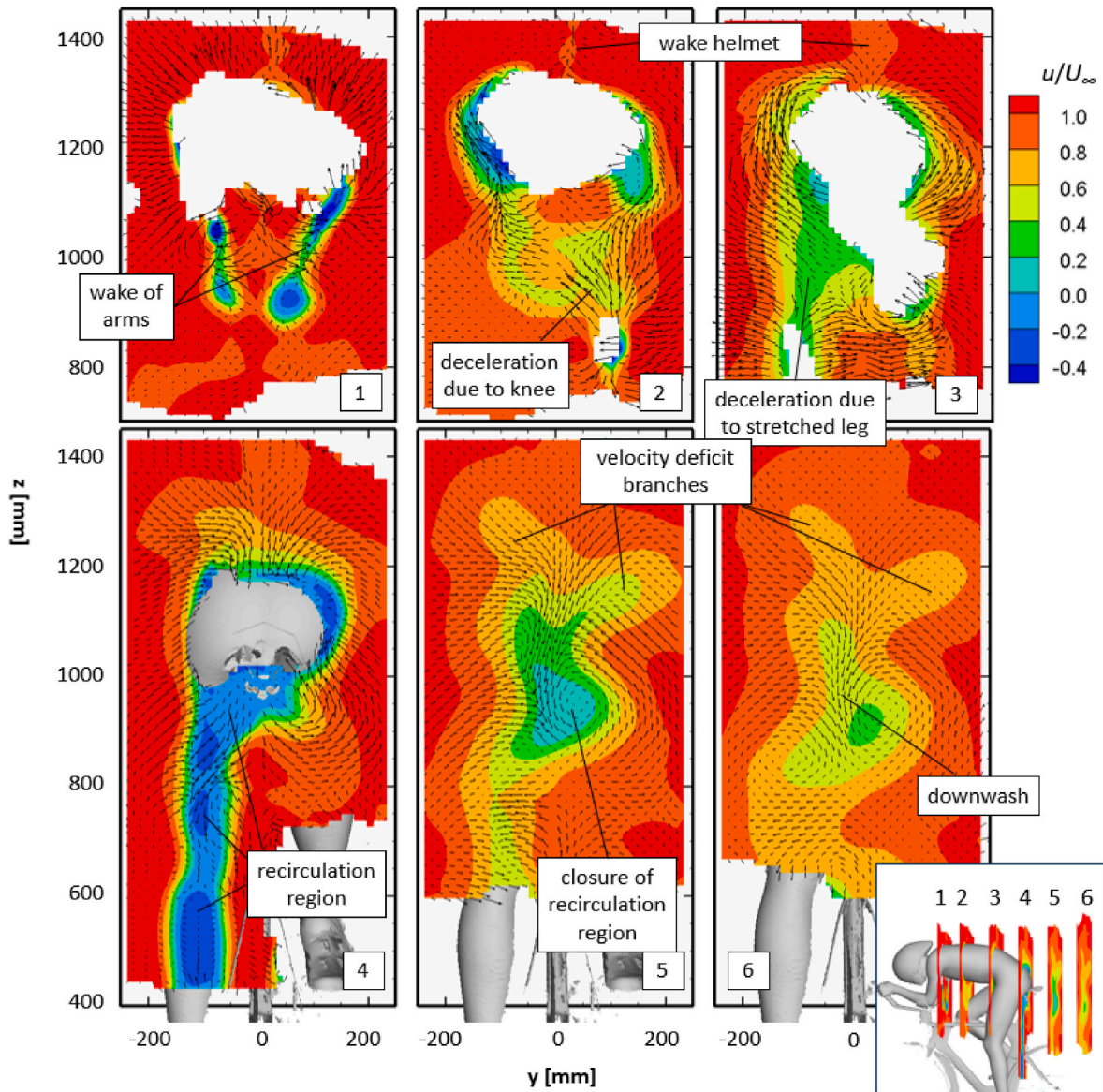

Fig. 11. Contours of streamwise velocity with in-plane vectors at $x = -350$ mm (1), $x = -200$ mm (2), $x = 0$ (3), $x = 200$ mm (4), $x = 400$ mm (5) and $x = 600$ mm (6).

(bottom) in the same cross-planes as those depicted in Fig. 11. The observed downwash just downstream of the saddle (plane 5) peaks at w^* = −0.45. The flow around the upper leg ($v^* = \pm0.45$) and the upwash around the torso (left side, $w^* = 0.7$; right side, $w^* = 0.4$), discussed earlier, are also clearly observed in the marked peaks of the lateral and vertical velocity component, respectively, in plane 3 ($x = 0$). In the most downstream plane, x = 600 mm, the peaks in the distribution of the three velocity components have decayed significantly through the turbulent dissipation process and are around $u^* = 0.35$, $v^* = \pm0.2$ and w^* = −0.3, respectively.

Fig. 13-top depicts iso-surfaces of streamwise vorticity ($\omega_x^* = \pm2$) from three different viewing angles. The streamwise and lateral range of the measurement region has been cropped to $x < 750$ mm and 600 mm $< y < 1370$ mm, respectively, so that the measurement noise in the vorticity does not blur the main flow structures. Fig. 13-bottom presents contours of streamwise vorticity in six cross-planes, like the previous figures. From the iso-surfaces, it is observed that the clockwise rotating vortex (in blue) emanating from the left inner thigh merges with the clockwise rotating left hip/upper arm vortex. Both vortex structures have been labelled in Fig. 13 and are observed in the cross-plane at x = 900 mm (Fig. 9b). The formation of the hip/upper arm vortex can be appreciated from the vorticity distributions at the bottom of Fig. 13. The shear layer that forms on the inside of the left upper arm (see plane 1) rolls up around the torso (plane 2) and the hip (plane 3). The same vortex interaction occurs on the cyclist's right side between the counterclockwise rotating hip/upper arm and inner thigh vortices (in red). Instead, here the hip/upper arm and thigh vortex merge further upstream, mainly because the right inner thigh vortex moves further upwards (in a positive y direction) as a consequence of the orientation of the right upper leg. The outer shear layer that separates from the left

upper arm (labelled in Fig. 13-top left-view) also swirls around the torso, similar to the inner shear layer, forming a region of positive vorticity (marked as well in plane 4 bottom figure) on top of the left hip/upper arm vortex. On the right side of the cyclist, the upper arm outer shear layer (right view top figure) does not swirl around the torso because of the interaction with the right upper leg. Instead, the formed region of negative vorticity remains below the hip and seems to dissipate upon interaction with the right hip/upper arm vortex.

In contrast to the present finding, and as discussed in the previous section, a vortex pair, counter rotating with the hip and thigh vortices (type *upwash* Fig. 10b), is present in the wake of the mannequin used by Brown et al. (2023) and Wang et al. (2022). The latter mannequin has relatively wide shoulders. It is hypothesized here, that, as a consequence of these broad shoulders, possibly in combination with the larger upper arm angle, the outer shear layers emanating from the upper arms are advected on top of the inner shear layers by the swirling flow around the torso, creating this counter-rotating vortex pair in the upper wake with an upwash in between. This evolution of the vortices seems to match well to the vortical structures presented by Wang et al. They, however, do not discuss this in detail and, so, further investigation is needed to better understand the differences between the vortex topologies. Artificially adapting the shoulder posture of the present GCM may allow further study into the effect of the shoulder width on the hip/upper arm vortices.

Finally, some smaller vortex structures are observed around the present TT mode. Streamwise vortices, for example, emanate from the elbows (labelled in Fig. 13 top and bottom). Counter rotating vortex pairs are typically formed below each elbow (Terra et al., 2020), which are observed downstream of the right elbow (best appreciated and labelled in plane 1, bottom figure). These right elbow vortices quickly
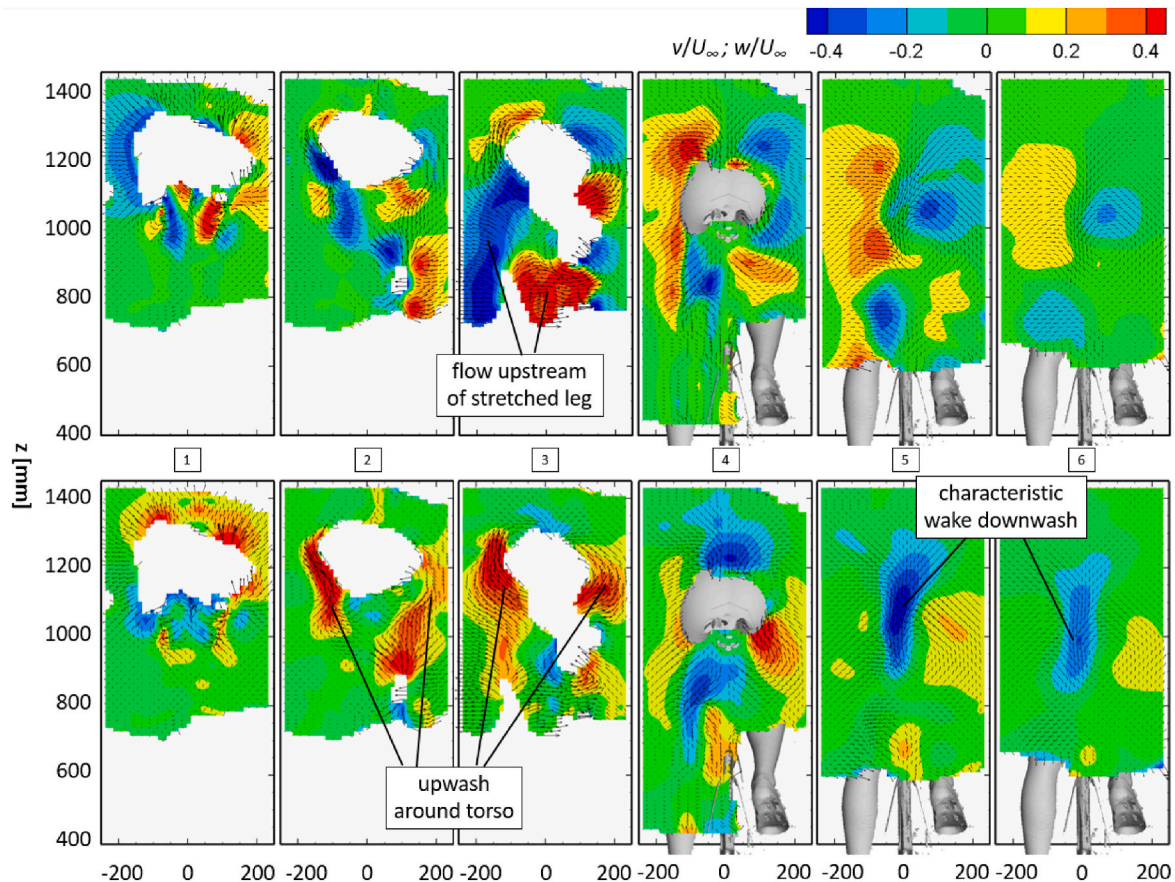

Fig. 12. Contours of normalized lateral, v, (top) and vertical, w, velocity (bottom) at $x = -350$ mm (1), $x = -200$ mm (2), $x = 0$ (3), $x = 200$ mm (4), $x = 400$ mm (5) and $x = 600$ mm (6).
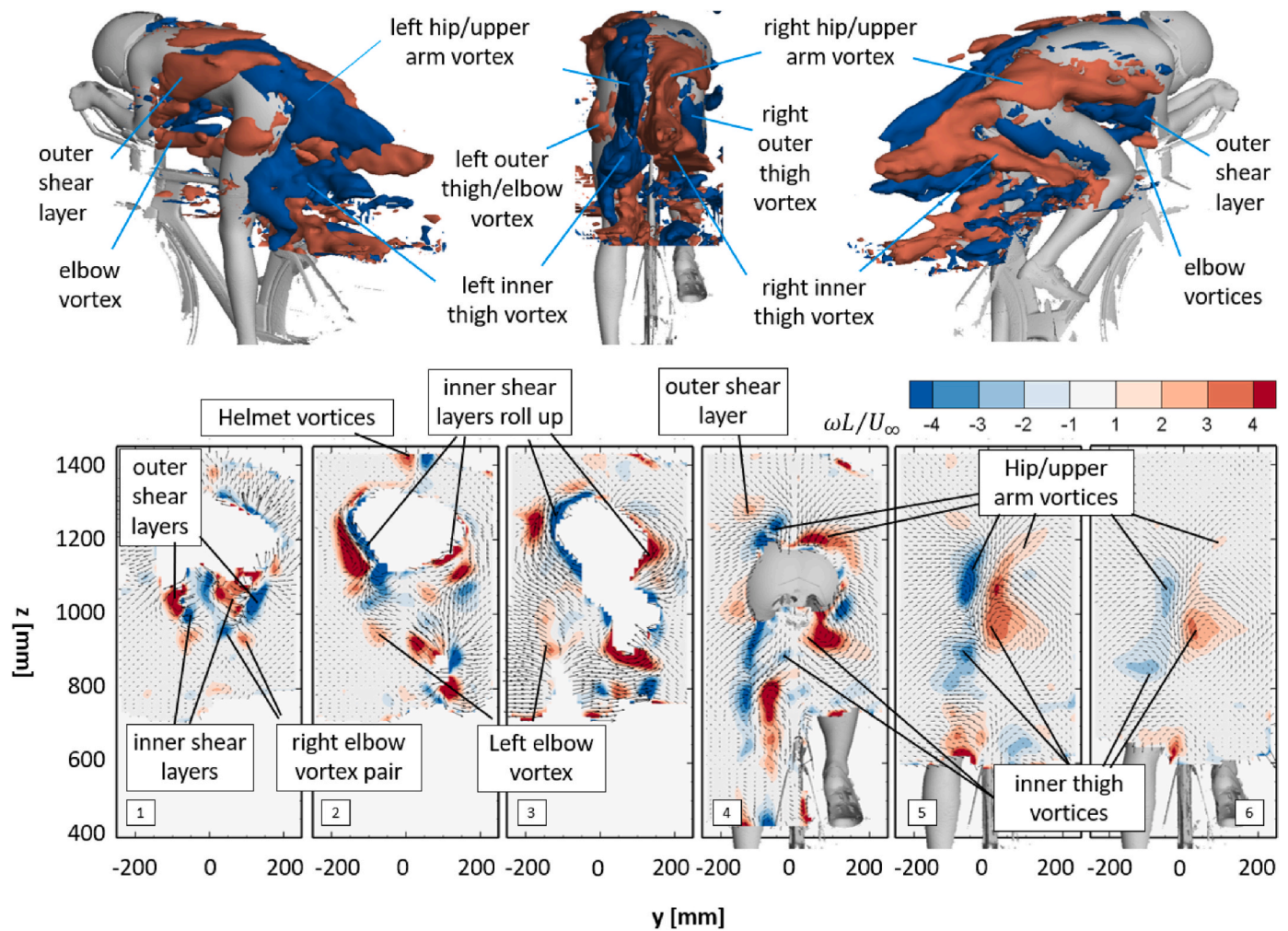
Fig. 13. Iso-surfaces of streamwise vorticity at $\omega_x^* = -2$ in blue and $\omega_x^* = 2$ in red (top) and contours of streamwise vorticity at x = −350 mm (1), x = −200 mm (2), x = 0 (3), x = 200 mm (4), x = 400 mm (5) and x = 600 mm (6) at the bottom.

interact with the flow around the right knee and cannot be identified anymore through the formation of the thigh vortices. On the left side of the mannequin, the clockwise rotating (blue) elbow vortex is missing, which is expected on the outside of the elbow, for reasons unclear to the authors. The inner vortex, instead, is clearly present and, after separation from the elbow it is advected downstream (marked in planes 2 and 3), merging with the left outer thigh vortex (labelled mid-view top figure). This left outer thigh/elbow vortex is rather weak in comparison to the right outer thigh vortex, because of the different orientation of the two upper legs. The last vortex pair that is mentioned here is that emanating from the helmet (marked in plane 2), generating a relatively weak upwash. As a consequence, this vortex pair detaches from the upper back and dissipates further downstream (not visible anymore in plane 4).

5. Discussion

In the previous section, the flows around the two generic cyclist models have been presented. Both models are static mannequins with the left leg stretched (high drag position). Significant differences in aerodynamic drag and wake topology between the sprint and time-trial positions are observed, which have been discussed and related to the literature. The two postures represent only a small portion of the different postures a cyclist can take on the bike. It is well known that other leg positions will feature different wake topologies (Crouch et al., 2014). Also (small) variations of the upper body, such as lower arm

angle and arm spacing, can have significant effects on the flow around it and, in turn, the aerodynamic drag (e.g. Giljarhus et al., 2020). Apart from the cyclist posture, the topology is also affected by the surface roughness (type of suit), the turbulence in the surrounding air (Brown et al., 2023). Despite the small number of parameters varied in the present work, the main goal of this research has been achieved: introducing a shared, representative cyclist model, that can be used freely by all, in combination with a benchmark velocity dataset. In the vision of the authors, this dataset is to be considered as part of a continuously growing database that is being expanded through future wind tunnel and numerical experiments. These newly studied GCM postures and the flow around them, again, will become available to the entire community, so to increase the rate at which our understanding of cycling aerodynamics advances. Similar to the dataset underlying the present work, each new dataset becomes part of the overarching database, a collection entitled *The Generic Cyclist Model for aerodynamic investigation* (Terra, 2024). The overarching collection also contains a description of managing newly added datasets.

A first addition to the collection will be the velocity data obtained from the 450 kW wind tunnel at Monash University, where the authors install the same time-trial GCM as in the present work, on the same bike, and the cyclist wake is scanned using a four-hole Cobra probe (e.g. Crouch et al., 2014, Brown et al., 2023). This addition will provide insight into the expected variations in wake topology when using different flow measurement techniques and testing in different wind tunnels and, in turn, this uncertainty provides a valuable benchmark for

future cyclist aerodynamic simulation using RANS, DES or LES.

After this, the authors plan to advance the database with CFD simulations of the present TT GCM in non-zero yaw, to better understand the effect of cross-winds on cycling aerodynamic. Also other GCM geometries and positions are foreseen. For the latter, it is possible to scan riders in new positions, similar to the present work. Although this procedure is very time intensive, it will be unavoidable when introducing a female cyclist model, which is one of our main goals, so to understand if the female anthropometric features affect the flow significantly different in comparison to a male rider. Re-scanning riders may be avoided when variations in posture of the present models is the topic of research. The model posture can be varied, for example, through virtual skeletal methods resulting in realistic human soft tissue deformation and, in turn, a realistic flow around it (Giljarhus et al., 2023). The resulting new outer geometry and the flow around can be added to the database. Ideally, also the procedure to change the position of the skeleton is prescribed, so that others may use these as well.

Finally, note that the authors do not expect the academic aerodynamic cycling community to use only the GCMs from now on. Specific cyclist replicas remain a topic of research to optimize for a specific rider or group of riders. However, with the information of the GCM available, one can relate the findings of these other models to those on the GCM, allowing other researchers also to advance on such results. The authors hope the community recognises the value of the present work, that they embrace the use of the generic cyclist models and help us advance the GCM database.

6. Conclusions

Two anthropometrically realistic Generic Cyclist Models (GCM) are introduced, which have been obtained by scanning a group of 14 elite cyclists in time-trial and sprint positions and averaging their body geometries. These average geometries are used to manufacture two full-scale mannequins that are installed in a wind tunnel to compare their wake flow topology. Robotic volumetric PIV is employed to obtain the time-average velocity in a thick plane about 1 m downstream of the bottom bracket. In addition, the flow all around the time-trial model is obtained to understand the origin of the dominating flow structures. The obtained velocity statistics and the generic cyclist models, both the original geometries as well as the scans of the physical wind tunnel models on their corresponding bikes, are published free of access, which is unique in the field of cycling aerodynamic research.

A comparative analysis of the wake of the two models shows remarkable differences in (1) the location of the peak streamwise velocity deficit, (2) the strength of the counter rotating hip/thigh vortex pair and (3) the streamwise vortex topology in the upper wake. These differences are associated with the difference in posture and position of the arms on the handlebars. A larger gap between the arms allows more air with high momentum to access the chest and the gap in between the thighs, resulting in a stronger hip/thighs vortex pair and a stronger downwash in between the vortices. The latter, in turn, displaces the peak velocity deficit further towards the floor.

The drag area of the sprint model, that features a larger gap in between the arms, exceeds that of the TT model by 15% ($C_DA_\text{sprint} = 1.15\ C_DA_{TT}$). Hence, is it presumed that a stronger hip/thigh vortex pair and a stronger downwash in between these vortices, caused by the large arm spacing, is related to a higher aerodynamic drag. On the other hand, it is observed that the two models exhibit similar aerodynamic drag coefficients over the entire range of Reynolds numbers considered in this work. In other words: the higher drag area of the sprint model stems entirely from the difference in frontal area. Future work remains necessary in order to better understand the relation between the aerodynamic drag, the rider position and the flow topology.

After relating the present GCM wake topologies to that observed in the literature, a classification of the streamwise vortex topology is presented for the mid-wake and the upper-wake, which are dominated by

the counter rotating hip/thigh and upper arm/hip vortex pair, respectively. The upper-wake is classified into *downwash*, *neutral* and *upwash*, depending on the type of the counter-rotating vortex pair that dominates the flow downstream of the lower back. The authors presume that the arm spacing and the shoulder width (relative to the hip width) are the governing parameters.

Analysis of the flow around the time-trial model, clarifies the origin of the different streamwise vortices. The inner shear layers that emanate from the upper arms roll up around the torso and detach from the hips forming the *hip/upper arm* vortices. These vortices merge further downstream with the *inner thigh* vortices forming the *hip/thigh* vortices. The two presumably merge further downstream when the hip/upper arms vortices detach further atop of the lower back. Similar to the inner shear layers, the outer shear layers that emanate from the upper arms also roll up around the torso. For the present models, these are relatively weak. However, when stronger, they can also dominate the upper-wake (type *upwash*).

CRediT authorship contribution statement

Wouter Terra: Writing – review & editing, Writing – original draft, Visualization, Validation, Software, Project administration, Methodology, Investigation, Formal analysis, Data curation, Conceptualization. **Christopher Brown:** Writing – review & editing, Visualization, Software, Methodology, Conceptualization. **Siward Vloemans:** Investigation, Data curation. **Max van der Waals:** Software, Investigation, Formal analysis, Data curation. **Andrea Sciacchitano:** Writing – review & editing, Supervision, Conceptualization. **David Burton:** Writing – review & editing, Supervision, Conceptualization. **Mark C. Thompson:** Writing – review & editing, Supervision. **Toon Huysmans:** Writing – review & editing, Visualization, Supervision, Software, Methodology, Data curation, Conceptualization.

Declaration of competing interest

The authors declare that they have no known competing financial interests or personal relationships that could have appeared to influence the work reported in this paper.

Data availability

The underlying data is published at the 4TU repository (Terra et al., 2024)

Acknowledgements

References

Ahmed, S.R., Ramm, G., Faltin, G., 1984. Some Salient Features of the Time-Averaged Ground Vehicle Wake. SEA: Technical Paper Series. International Congress & Exposition, Detroit. Michigan, February 27-March 2.

Aider, J.L., Beaudoin, J.F., Wesfreid, J.E., 2009. Drag and lift reduction of a 3D bluff-body using active vortex generators. Exp. Fluid 48, p771–789.

Barlow, J.B., Rae, W.H., Pope, A., 1999. Low-speed Wind Tunnel Testing. OCLC: 39335023, third ed. Wiley, New York. ISBN: 978-0-471-55774-6.

Barry, N., Burton, D., Sheridan, J., Thompson, M., Brown, N.A.T., 2016. Flow field interactions between two tandem cyclists. Exp. Fluid 57 (12), 181.

Blocken, B., Defraeye, T., Koninckx, E., Carmeliet, J., Hespel, P., 2013. CFD simulations of the aerodynamic drag of two drafting cyclists. Comput. Fluids 71, 435–445.

Blocken, B., et al., 2018. Aerodynamic drag in cycling pelotons: new insights by CFD simulation and wind tunnel testing. J. Wind Eng. Ind. Aerod. 179, 319–337.

Brown, C., Crouch, T.N., Burton, D., Thompson, M.C., 2020. Understanding the aerodynamic benefits of drafting in the wake of cyclists. Proceedings 49, 32.

Brown, C., Burton, D., Crouch, T.N., Thompson, M.C., 2023. The influence of turbulence on cycling aerodynamics. J. Wind Eng. Ind. Aerod. 242, 105575.

Brownlie, L.W., 1992. Aerodynamic Characteristics of Sports Apparel. National Library of Canada. PhD thesis.

Brownlie, L.W., Kyle, C., Carbo, J., Demarest, N., Harber, E., MacDonald, R., Nordstrom, M., 2009. Streamlining the time trial apparel of cyclists: the Nike Swift Spin project. Sports Technol. 2, 53–60.

Chi, S., Pitman, J., Crouch, T.N., Burton, D., Thompson, M.C., 2020. The application of body scanning, numerical simulations and wind tunnel testing for the aerodynamic development of cyclists. Proc IMechE Part P: J Sports Eng Tech 1–15.

Crouch, T.N., Burton, D., Brown, N.A.T., Thomson, M.C., Sheridan, J., 2014. Flow topology in the wake of a cyclist and its effect on aerodynamic drag. J. Fluid Mech. 748, 5–35.

Crouch, T.N., Burton, D., Thompson, M.C., Brown, N.A.T., Sheridan, J., 2017. Riding against the wind: a review of competition cycling aerodynamics. Sports Eng. 20, 81–110.

Dyke, R.M., Lai, Y.K., Rosin, P.L., Zappala, S., et al., 2020. Shrec'20: shape correspondence with non-isometric deformations. Comput. Graph. 92, 28–43.

Garimella, R., Beyers, K., Huysmans, T., Verwulgen, S., 2020. Rigging and Re-posing a human model from standing to cycling configuration. In: Di Nicolantonio, M., Rossi, E., Alexander, T. (Eds.), Advances in Additive Manufacturing, Modeling Systems and 3D Prototyping. AHFE 2019, Advances in Intelligent Systems and Computing, 975.

Giaquinta, D., 2018. The Flow Topology of the Ahmed Body in Cross-Wind. Delft University of Technology, Department of Aerospace Engineering. MSc Thesis.

Gibertini, G., Grassi, D., 2008. Cycling aerodynamics. In: Nørstrud, H. (Ed.), Sport Aerodynamics, 506. Springer, Vienna, pp. 23–47.

Giljarhus, K.E.T., Stave, D.A., Oggiano, L., 2020. Investigation of influence of adjustments in cyclist arm position on aerodynamic drag using computational fluid dynamics. Proceedings 49, 159.

Giljarhus, K.E.T., Liland, F.F., Oggiano, L., 2023. Virtual skeleton methodology for athlete posture modification in CFD simulations. Sports Eng. 26, 39, 2023.

Griffith, M.D., Crouch, T.N., Thompson, M.C., Burton, D., Sheridan, J., Brown, N.A., 2014. Computational fluid dynamics study of the effect of leg position on cyclist aerodynamic drag. J. Fluid Eng. 136 (10), 101105.

Hanfeng, W., Yu, Z., Chao, Z., 2016. Aerodynamic drag reduction of an Ahmed body based on deflectors. J. Wind Eng. Ind. Aerod. 148, 34–44.

Heft, A., Indinger, T., Adams, N., 2012. Introduction of a new realistic generic car model for aerodynamic investigations. SAE Technical Paper 2012-01-0168.

Huysmans, T., Goto, L., Molenbroek, J., Goossens, R., 2020. DINED mannequin. Tijdschr. Hum. Factors 45, 4–7.

Jux, C., Sciacchitano, A., Scarano, F., 2023. Tire dependence for the aerodynamics of yawed bicycle wheels. J. Wind Eng. Ind. Aerod. 233, 105294.

Jux, C., Sciacchitano, A., Schneiders, J.F.G., Scarano, F., 2018. Robotic volumetric PIV of a full-scale cyclist. Exp. Fluid 59, 74.

Kazhdan, M., Hoppe, H., 2013. Screened Poisson surface reconstruction. ACM Trans. Graph. 32 (3), 1–13.

Lignarolo, L.E.M., Ragni, D., Krishnaswami, C., Chen, Q., Simao Ferreira, C.J., Van Bussel, G.J.W., 2014. Experimental analysis of the wake of a horizontal-axis wind turbine model. Renew. Energy 70, 31–46.

Malizia and Blocken, 2021. Cyclist aerodynamics through time: better, faster, stronger. J. Wind Eng. Ind. Aerod. 214, 104–673.

Mancewicz, J., Derksen, M.L., Rijpkema, H., Wilson, C.A., 2014. Delta mush: smoothing deformations while preserving detail. In: Proceedings of the Fourth Symposium on Digital Production, pp. 7–11.

Oggiano, L., Brownlie, L., Troynikov, O., Bardal, L.M., Sæter, C., Sætran, L., 2013. A review on skin suits and sport garment aerodynamics: guidelines and state of the art. Procedia Eng. 60, 91–98.

Puelles, Magan G., Terra, W., Sciacchitano, A., 2021. Aerodynamics analysis of speed skating helmets: investigation by CFD simulations. Appl. Sci. 11, 3148.

Schanz, D., Gesemann, S., Schroeder, A., 2016. Shake the Box: Lagrangian particle tracking at high particle image densities. Exp. Fluid 57–70.

Shanebrook, J.R., Jaszczak, R.D., 1974. Aerodynamics of the human body. In: Nelson, R. C., Morehouse, C.A. (Eds.), Biomechanics IV. International Series on Sport Sciences. Palgrave, London.

Terra, W., Sciacchitano, A., Scarano, F., 2019. On the Cyclist's drag crisis. J. Sci. Cycl. 8 (2), 57–58.

Terra, W., Sciacchitano, A., Scarano, F., 2020. Cyclist Reynolds number effects and drag crisis distribution. J. Wind Eng. Ind. Aerod. 200, 104–143.

Terra, et al., 2024. A Generic Cyclist Model for aerodynamic investigation: Design, geometry & first aerodynamic analysis of a male time-trial and sprint model (Underlying Data). 4TU Repository. https://doi.org/10.4121/a6bafb56-588e-40c d-a304-4a1cd61a312d.

Terra, W., 2024. A Generic Cyclist Model for Aerodynamic Investigation. 4TU Repository. https://doi.org/10.4121/1fff941e-cbcc-485b-8b5f-7f8c0899e131.

Wang, S., Pitman, J., Brown, C., Tudball Smith, D., Crouch, T.N., Thompson, M.C., Burton, D., 2022. The influence of the inter-relationship of leg position and riding posture on cycling aerodynamics. Fluid 7, 1.

Wood, R., 2015. Anthropometry and cycling. Topend Sports. Retrieved from. http s://www.topendsports.com/sport/cycling/anthropometry.htm.

Zhang, C., Tanneberger, M., Kuthada, T., Wittmeier, F., et al., 2019. Introduction of the AeroSUV-A New Generic SUV Model for Aerodynamic Research. SAE Technical Paper 2019-01-0646.